AIAA JOURNAL
Vol. 51, No. 11, November 2013

Compensation of Nonlinear Harmonic Coupling for Pulsed-Jet-Velocity Shaping

Cory Hendrickson* and Robert M'Closkey†
University of California, Los Angeles, California 90095

DOI: 10.2514/1.J052241

This paper describes an approach to periodic reference tracking in a pulsed-jet-injection experimental study. The objective was to match the jet's temporal velocity profile to a periodic reference. The challenge lies in controlling the highly nonlinear and poorly understood dynamics associated with the jet velocity. Although the actuator maintains good authority over the jet velocity, the nonlinear jet dynamics creates a high degree of coupling among neighboring harmonics that depends on the forcing level and the desired waveform. The coupling is quantified by demodulating the jet-velocity measurement into baseband components centered at the harmonic frequencies represented in the desired waveform. An empirical input–output relationship is developed by perturbing the baseband components and measuring their effect on neighboring harmonics, and it is shown that this relationship can be modeled as a linear multi-input/multi-output system. This knowledge is exploited to create stabilizing feedback controls that asymptotically drive the jet velocity to the desired waveforms over a wide range of forcing conditions.

Nomenclature

a_k, b_k	=	Fourier coefficients of desired waveform
$\tilde{C}_p$	=	pressure-loop controller, demodulated coordinates
$\tilde{C}_v$	=	velocity-loop controller, demodulated coordinates
$\tilde{e}_v$	=	velocity tracking error, demodulated coordinates
g_p, g_v	=	pressure- and velocity-loop scalar gains
H	=	Laplace transform of h
$\tilde{H}$	=	H with quadrature input columns removed
H_{lp}	=	single-input/single-output low-pass filter following demodulation blocks
$H(0)$	=	dc component of H
h	=	matrix impulse response from δ_p to δ_v
j	=	$\sqrt{-1}$
K_v	=	velocity-controller-gain matrix
L_p	=	scalar loop gain of pressure-feedback loop
n_e	=	number of samples used for identifying $H(0)$
n_h	=	number of modulation/demodulation blocks (number of controlled harmonics)
n_p	=	number of operating points used in controller synthesis
$\tilde{P}_p$	=	demodulated plant with pressure output
$\tilde{P}_v$	=	demodulated plant with velocity output
P_d, P_x	=	scalar transfer functions associated with $\tilde{P}_p$
$\mathbb{R}^{m\times n}$	=	$m \times n$ matrices with real elements
R_k, I_k	=	pressure-controller compensation constants at frequency $k\omega_0$
$\tilde{r}_p$	=	pressure reference
$\bar{r}_p$	=	constant portion of pressure reference
$\bar{r}_v$	=	constant portion of velocity reference
t	=	time
t_s	=	sample period
$\tilde{u}$	=	input vector for demodulated plants $\tilde{P}_p$ and $\tilde{P}_v$
u_n^i, u_n^q	=	in-phase and quadrature elements of $\tilde{u}$
V_{rms}	=	velocity rms amplitude
$\mathbf{x}$	=	state vector of h
$\mathbf{x}_v$	=	velocity-controller-state vector
y_p, y_v	=	pressure and velocity outputs, scalar valued
$\tilde{y}_p$, $\tilde{y}_v$	=	demodulated pressure and velocity signals, vector valued
$y_{p,k}^i$, $y_{p,k}^q$	=	in-phase and quadrature components of $\tilde{y}_p$ at frequency $k\omega_0$, scalar valued
y_{ref}	=	velocity-reference waveform, scalar valued
$\bar{y}_v$	=	mean value of $\tilde{y}_v$
$y_{v,n}^i$, $y_{v,n}^q$	=	in-phase and quadrature components of $\tilde{y}_v$ at frequency $k\omega_0$, scalar valued
α	=	maximum-singular-value limit for K_v
β_k	=	constraint matrices in controller synthesis
γ	=	generalized eigenvalue
γ^*	=	minimum achievable generalized eigenvalue
Δ_p, Δ_v	=	vector-valued time series of δ_p and δ_v for identification of $H(0)$
δ_p	=	perturbation summed with pressure reference $\bar{r}_p$
δ_v	=	time-varying portion of $\tilde{y}_v$
$\delta_{v,k}^i/\delta_{p,l}^i$	=	transfer function relating the in-phase components of lth input channel and kth output channel of H
λ_{cl}	=	closed-loop eigenvalues
$\bar{\sigma}(\cdot)$	=	maximum singular value
ω_c	=	H_{lp} corner frequency
ω_0	=	fundamental frequency of y_{ref}
$\lvert\cdot\rvert$	=	absolute value
$\lVert\cdot\rVert_2$	=	Euclidean norm
$(\cdot)^T$	=	matrix transpose

I. Introduction

UNDERSTANDING the dynamics of jets injected into quiescent surroundings or into crossflows is a fundamental problem with application to a wide range of engineering systems, particularly those for propulsion and energy generation [1,2]. Transverse jets appear in airbreathing turbine engines as dilution air jets, which reduce the temperature pattern factor downstream of combustion, and for turbine-blade cooling, in which air injected from the leading edge insulates the turbine blade from the hot surrounding combustion gases. The active control of jet injection has been shown to improve the important characteristics of each flowfield such as spread and penetration of the jet into the crossflow for dilution jet injection [3] and boundary-layer attachment at low turbine inlet Reynolds numbers for turbine-blade cooling [4]. The control of the jet in the crossflow is typically accomplished through temporal excitation of the jet fluid using flow-rate modulation or acoustic forcing [5–8]. The excitation is periodic, usually with the goal of forming either sinusoidal or pulselike jet-velocity profiles. Pulsed jets have been

Received 27 July 2012; revision received 2 February 2013; accepted for publication 6 May 2013; published online 16 September 2013.

*Graduate Student, Department of Mechanical and Aerospace Engineering.

†Professor, Department of Mechanical and Aerospace Engineering.

noted to form strong vortex rings that penetrate greatly into the crossflow, leading to enhanced mixing [9].

Feedback control is required to shape the jet velocity because open-loop methods are subject to errors as a result of flow disturbances and uncertainty associated with the system dynamics [7,8]. The field of repetitive control, which addresses the asymptotic disturbance rejection and reference tracking of periodic signals, provides a framework for pulsed-jet reference tracking. All forms of repetitive control are based on the internal model principle, which requires a model of the disturbance or reference to be included in the feedback loop for perfect rejection or tracking [10]. Systems based on repetitive control commonly use a time delay in the feedback loop to place an infinite number of poles on the imaginary axis at the fundamental frequency and harmonics of the periodic disturbance or reference [11–13]. In practice, the plant has finite bandwidth and the controller is implemented with a digital signal processor; therefore, only a finite number of internal models can be created for asymptotic tracking. In this case, modulated–demodulated control can be used as an alternative to time-delay repetitive control [14,15]. The modulated–demodulated control, also referred to as adaptive feedforward control or adaptive feedforward cancellation [16,17], demodulates the spectrum of a wideband signal into a family of baseband signals, operates at baseband, and then modulates the baseband spectra back to higher frequency.

The plant represents the dynamic system from the actuator command to the hot-wire-anemometer measurement taken at the jet exit, and "baseband" refers to a narrow frequency band, typically 10–50 Hz, centered at 0 Hz that represents the jet-velocity behavior in a neighborhood of each of the demodulation frequencies. The periodic jet-velocity waveforms at amplitudes exceeding 0.5 ms^{-1} rms exhibit nontrivial coupling among the harmonics that can destabilize the closed-loop system employing a controller designed for more moderate forcing amplitudes. The authors' past research addressed lower-amplitude forcing, in which linear models of the jet velocity were adequate for control design [18]. Research works on pulsed jets using primarily open-loop control schemes are presented in [5–8]. In the present study, we show that identification of the plant dynamics in the baseband coordinate system provides key insight into the nonlinearity that couples adjacent frequency bins under strong forcing conditions. The baseband coordinates also provide a convenient framework for compensating the harmonic coupling. In fact, the nonlinear coupling can be modeled in the baseband coordinates as a multi-input/multi-output (MIMO) constant gain. This control strategy achieves asymptotic tracking of the desired jet-velocity waveform within the bandwidth of the actuation system. An inner equalizing control loop that feeds back the plenum-pressure measurement is also employed to equalize the magnitude of the jet-velocity response and to reduce the condition number of the jet-velocity gain matrix. The identification and control strategy detailed here provides a framework to explore how precise jet-velocity waveforms improve mixedness, penetration, and spread compared to open-loop control schemes; however, these studies are not yet complete, and will be reported elsewhere.

II. Pulsed-Jet Experiment

A. Actuation System

A schematic of the experimental pulsed-jet-injection apparatus is shown in Fig. 1. Compressed air, regulated to maintain a constant mean jet velocity of 8 ms^{-1}, flows into a plenum, and then through a smoothly contracted nozzle into quiescent surroundings. The nozzle is brought to an approximately 4 mm exit diameter by a fifth-order polynomial contraction, resulting in a nearly top-hat spatial velocity profile with a measured scaled moment thickness $D/\theta = 26$. The jet Reynolds number, based on the mean jet velocity, is held constant at 2000. The jet velocity is perturbed about its 8 ms^{-1} mean value by a lightweight piston positioned at the bottom of the plenum. The piston is driven in-line with the jet by a modal shaker (Ling Electronics LVS-100). The shaker voice-coil current is proportional to the shaker amplifier-input signal, the latter being the plant input. The jet velocity is measured using a hot-wire anemometer (Dantec 54T30) placed in

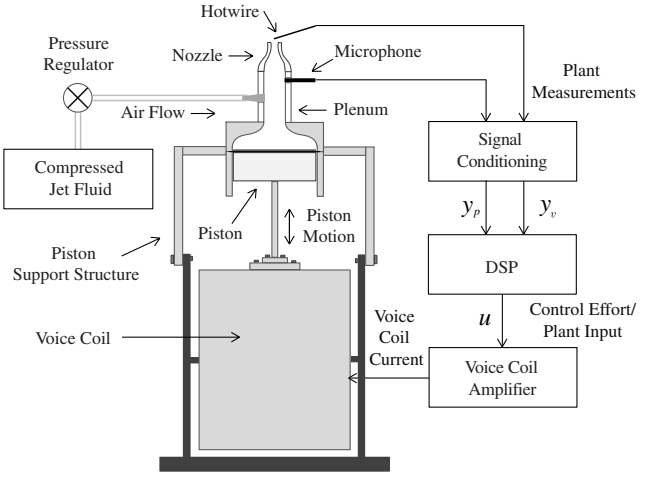

Fig. 1 Pulsed-jet injection experimental setup.

the center of the jet at the nozzle exit. Additionally, the apparatus is equipped with a microphone (PCB Piezotronics 378C01) that measures the pressure at the top of the plenum. Controllers are implemented in MATLAB's xPC Target application with a 25 kHz sampling rate [19]. Eight-pole, low-pass Chebyshev filters with 10 kHz corner frequencies are used as antialias filters for filtering the microphone and hot-wire signals before sampling. The entire system can be placed beneath a wind tunnel with the nozzle-exit flush with the test-section floor if a crossflow is desired. An industrial blower driven by an adjustable-speed electric motor introduces the crossflow, and several screens and a honeycomb flow-straightener section condition the crossflow before entering the test section, which is 12×12 cm in cross section and 30 cm in length. This apparatus has been employed in a wide range of unforced [20,21] and forced experimental studies [6–8,18,22], in which the jet-to-crossflow velocity ratio varies between 1.15 and 10, and the jet-to-crossflow density ratio varies between 0.14 (pure helium) and 1.00 (pure air). In the present study, the control technique is demonstrated without a crossflow.

B. Motivation: Nonlinear Coupling Between Harmonics

Linear models of the pulsed jet can be developed from data generated with low-amplitude test inputs. Controllers developed using the models are then adequate for low-amplitude reference tracking [18,22]. At forcing amplitudes exceeding 0.5 ms^{-1} rms though, the nonlinear response of the velocity measurement (the regulated variable) can destabilize the closed-loop system. The desired velocity perturbation is periodic, and so the nonlinear response can be studied from the point of view of coupling among harmonics in the periodic waveform. The magnitude and character of the harmonic coupling are dependent upon the desired velocity reference and the rms forcing level.

In general, the nonlinear dynamics alter the estimated velocity frequency response according to the system's particular identification input. For example, the velocity frequency response, shown in Fig. 2, is measured using band-limited white-noise inputs with amplitudes set to perturb the jet velocity by 0.15 ms^{-1} rms (solid line) and 0.80 ms^{-1} rms (dashed line). The frequency response is determined by averaging the cross spectra of the input–output data, and then normalizing by the input power spectrum [23]. It is evident that the frequency response derived from the case with harder forcing deviates from the low-amplitude frequency response. Additionally, the jet-velocity coherence, shown in Fig. 3, decreases with the higher-amplitude forcing compared to the nominal case. The coherence is reduced because a greater portion of the velocity output is determined by nonlinear dynamics at higher forcing amplitudes. In contrast, the frequency responses with the pressure measurement are nearly identical for both test amplitudes and, furthermore, Fig. 3 shows the pressure coherence increases with harder forcing (the expected response of a linear plant with an additive fixed disturbance/noise spectrum).

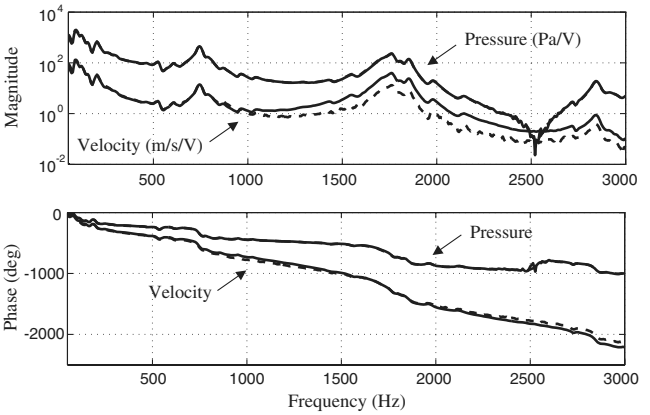

Fig. 2 Velocity and pressure frequency responses when $V_{\text{rms}} = 0.15$ ms^{-1} (solid) and $V_{\text{rms}} = 0.80$ ms^{-1} (dash).

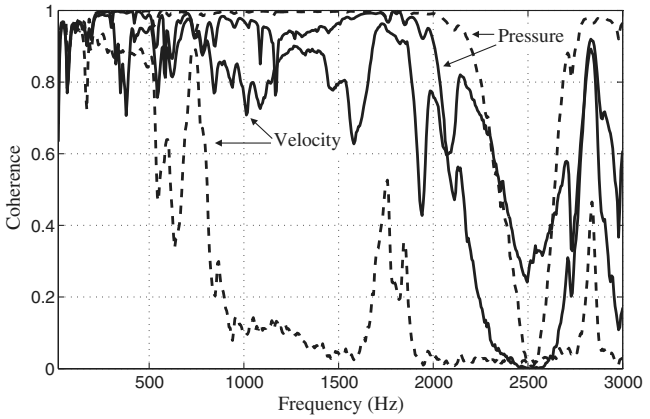

Fig. 3 Coherence of the empirical frequency response data in Fig. 2.

The jet response to dual-tone forcing clearly demonstrates jet-velocity nonlinearity and the difficulty it presents for periodic reference tracking. Figure 4 shows the velocity spectra in response to dual-tone forcing at 1800 and 1900 Hz with an amplitude that perturbs the jet velocity by $V_{\text{rms}} = 0.50$ ms^{-1}. The inputs at 1800 and 1900 Hz produce strong super- and subharmonics occuring at integer multiples of 100 Hz, which is the difference between the two input tones. The figure also shows the pressure spectrum in response to the same dual-tone input — the pressure measurement is dominated by tones at 1800 and 1900 Hz, which supports the hypothesis that the pressure responds in an essentially linear manner to the input.

The harmonics generated under periodic forcing make it difficult to determine the open-loop forcing conditions which will produce the desired periodic velocity waveform. This motivates using hot-wire feedback; however, the controllers must explicitly account for the coupling between harmonics. This paper introduces an approach for identifying the coupling and a feedback-compensation strategy that permits asymptotic tracking of the reference waveform for very large perturbations relative to the mean velocity.

III. Identification of Harmonic Coupling

The frequency responses in Fig. 2 show that the magnitudes roll off after a plenum mode near 1.8 kHz. This limits the actuation bandwidth to approximately 2.0 kHz. As such, we specify the periodic reference to be truncated at or below 2.0 kHz to avoid saturation of the actuator amplifier. Throughout this paper, the reference waveforms have a fundamental frequency $\omega_0 = 100$ Hz, and so modulation/demodulation is centered in narrow bands around the frequencies $k\omega_0$, $k = 1, 2, \ldots, n_h$, within the actuation bandwidth. The integer n_h denotes the number of frequency bands, and in this study, $n_h = 20$. Although the disturbance spectrum will only be attenuated in a neighborhood of each harmonic, the primary

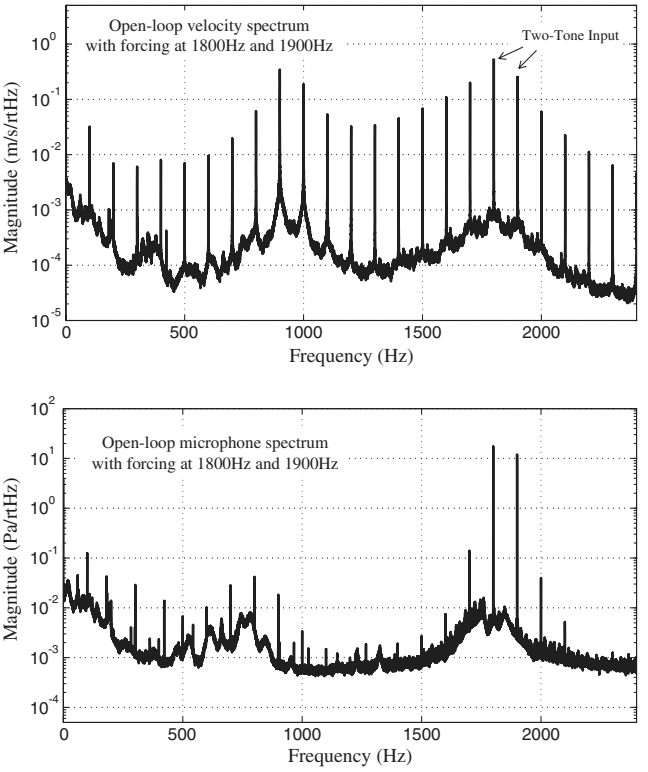

Fig. 4 Velocity response (top) and pressure response (bottom) to dual-tone forcing.

reason for using hot-wire-anemometer feedback to shape the jet velocity is the uncertainty associated with the plant dynamics. It is not possible to identify a plant model of sufficiently high fidelity that its inverse provides the correct open-loop forcing conditions; thus, feedback is used to force the jet velocity to asymptotically track the periodic reference within the actuator bandwidth, even in the presence of the significant coupling noted in Fig. 4.

The physical mechanisms causing the nonlinear harmonic coupling are not well understood; however, empirical models can be identified that are quite suitable for synthesizing stabilizing controllers. We identify models which characterize the harmonic coupling in a neighborhood of a particular periodic jet-velocity operating point that is close to the desired periodic waveform. As the character of the harmonic coupling depends upon the reference waveform, multiple models must be identified for controller synthesis when tracking references at operating points that are sufficiently far from one another.

A. Modulated–Demodulated Control

At a given operating point, the main challenge in modeling the system is quantifying the nonlinear coupling that occurs between the n_h frequency bins of the hot-wire signal and the n_h frequency bins of the input signal. The identification is facilitated by shifting the spectrum of the plant's input and output in the neighborhood of each harmonic to baseband via modulation and demodulation. Figure 5 shows the block diagrams of both of these processes. The modulation block has $2n_h$ baseband inputs, the low-bandwidth in-phase and quadrature signals, denoted $u_k^i(t)$ and $u_k^q(t)$ $(k = 1, 2, \ldots, n_h)$. These scalar signals are assembled into the vector $\tilde{u}$ and ordered according to Fig. 5. The baseband inputs are modulated by cosines and sines at n_h harmonics of the periodic reference, and summed to form the wideband control effort u. The demodulation block demodulates the wideband signal y with cosines and sines at the same frequencies. The demodulated signals are low-pass filtered by H_{lp} to form the low-bandwidth in-phase and quadrature signals $y_k^i(t)$ and $y_k^q(t)$ $(n = 1, 2, \ldots, n_h)$. These signals are assembled into the vector $\tilde{y}$. In the sequel, subscripts on the vectors or their elements denote the associated measurement. The variable v denotes the velocity

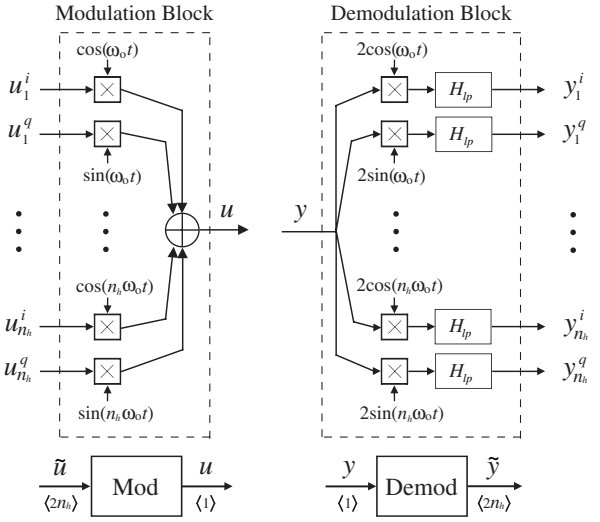

Fig. 5 Modulation and demodulation operations. Signal dimensions are shown between brackets ⟨ ⟩.

measurement from the hot-wire anemometer, and p denotes the pressure measurement from the microphone. The low-pass-filter corner frequency is chosen $\omega_c < \omega_0/2$ because this prevents any direct overlap of, and interaction between, adjacent frequency channels as a consequence of the signal processing. Coupling is present, however, due to the dynamics of the jet.

The modulation and demodulation blocks transform the pressure and velocity plants into $2n_h$-input/$2n_h$-output systems as shown in Fig. 6 for the pressure plant. The systems from $\tilde{u}$ to $\tilde{y}_p$ and from $\tilde{u}$ to $\tilde{y}_v$ are denoted $\tilde{P}_p$, the pressure plant, and $\tilde{P}_v$, the velocity plant, respectively. Note that, because P_p is well modeled as a linear system, $\tilde{P}_p$ is block diagonal in the sense that all transfer functions relating the input–output pairs for differing frequencies are essentially zero and can be neglected in the analysis [18]. Nonzero transfer functions relating the input–output pairs at the same frequency are arranged in 2×2 blocks on the diagonal of $\tilde{P}_p$. Provided

$$|H_{lp}(j\omega)| \approx 0 \quad \text{for} \quad \omega > \omega_c$$

the kth 2×2 block on the diagonal can be represented by a two-input/two-output linear time-invariant system with the transfer function possessing the following structure:

$$\tilde{P}_{p,k}(s) = \begin{bmatrix} P_d(s) & P_x(s) \\ -P_x(s) & P_d(s) \end{bmatrix}, \qquad k = 1, \ldots, n_h \tag{1}$$

in which the scalar transfer functions are

$$P_d(s) = \frac{1}{2} H_{\text{lp}}(s)[P_p(s + jk\omega_0) + P_p(s - jk\omega_0)]$$

$$P_x(s) = \frac{j}{2} H_{\text{lp}}(s)[P_p(s + jk\omega_0) + P_p(s - jk\omega_0)]$$

In other words, in modulated–demodulated coordinates, the transfer function with the pressure-measurement output is

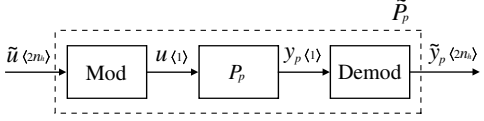

Fig. 6 Diagram of MIMO pressure system.

$$\tilde{P}_p = \begin{bmatrix} \tilde{P}_{p,1} & 0 & \ldots & 0 \\ 0 & \tilde{P}_{p,2} & & \vdots \\ \vdots & & \ddots & 0 \\ 0 & \ldots & 0 & \tilde{P}_{p,n_h} \end{bmatrix} \tag{2}$$

In contrast, $\tilde{P}_v$ is nonlinear and dependent upon the operating point. We will demonstrate, however, that in a neighborhood of an operating point, $\tilde{P}_v$ can be modeled as an affine function of the input. The transformation to baseband coordinates permits the characterization of the nonlinear harmonic-coupling phenomenon in a linear framework, which simplifies identification and control.

B. Inner Loop with Pressure Feedback

The pressure signal is essentially independent of the operating point, and it is convenient to close an inner loop using this measurement for two reasons. First, a stable operating condition can be established by specifying the reference values for the demodulated-pressure signal components. The pressure-reference values can be chosen to produce the jet-velocity components that are close to the desired periodic jet-velocity components. Indeed, if the pressure references could be chosen to exactly produce the desired jet velocity, then feedback of the hot-wire-anemometer signal would not be necessary; however, due to imprecise knowledge of the jet-velocity plant, it is not possible to choose the references in an open-loop manner so as to produce the desired jet-velocity waveform. Nevertheless, the operating point created using the plenum-pressure feedback provides a useful steady-state periodic velocity signal, which is close to the desired waveform and about which a small-signal model of the jet velocity can be developed. The second reason for using an inner pressure-feedback loop is the equalizing effect it has on the demodulated components of the jet velocity relative to the pressure-reference values. The equalization is useful because it vastly reduces the condition number of the empirically derived map from the pressure reference to the demodulated components of the jet velocity. The reduced condition number makes the control schemes described in Sec. IV more robust to errors in the identified model when the hot-wire measurement is used for feedback.

The inner loop is closed around P_p using the modulated–demodulated control method described in [18], and the inner-loop controller has the same block-diagonal structure as $\tilde{P}_p$:

$$\tilde{C}_p = \begin{bmatrix} \tilde{C}_{p,1} & 0 & \ldots & 0 \\ 0 & \tilde{C}_{p,2} & & \vdots \\ \vdots & & \ddots & 0 \\ 0 & \ldots & 0 & \tilde{C}_{p,n_h} \end{bmatrix}$$

The closed-loop block diagram is shown in Fig. 7. The reference for this loop is $\tilde{r}_p$:

$$\tilde{r}_p = [r^i_{p,1}, r^q_{p,1}, \ldots r^i_{p,n_h}, r^q_{p,n_h}]^T$$

in which the superscripts i and q denote the in-phase component and quadrature component, respectively. Figure 8 shows the kth 2×2 block on the diagonal of $\tilde{C}_p$. The integrators provide zero steady-state tracking error for constant references, and thus, the transfer function from $\tilde{r}_p$ to $\tilde{u}$ inverts $\tilde{P}_p$ at $\omega = 0$. When this inverse is cascaded with $\tilde{P}_v$, the relationship between $\tilde{y}_v$ and $\tilde{r}_p$ does not suffer from the large gain variations in the block-diagonal terms.

The fixed gains R_k and I_k invert the phase of P_p at frequency $k\omega_0$ for phase compensation; specifically, R_k and I_k are defined according to

$$R_k + jI_k = \frac{P_p(jk\omega_0)}{|P_p(jk\omega_0)|} \tag{3}$$

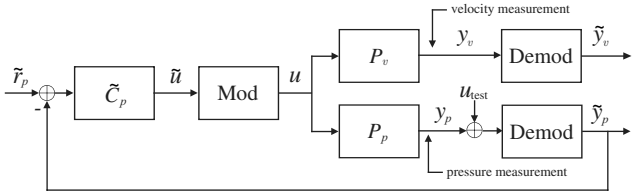

Fig. 7 Block diagram for identification of harmonic coupling.

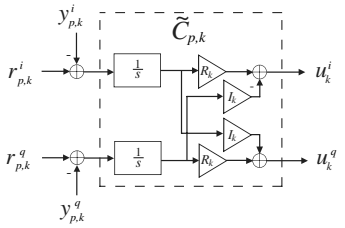

Fig. 8 Block diagram of the two-input/two-output kth channel of $\tilde{C}_p$.

If the loop is broken at y_p in Fig. 7, the scalar loop gain can be represented as a set of n_h linear time-invariant subsystems in parallel connection, each with loop gain:

$$L_{p,k}(s) = g_{p,k}P_p(s) \times \left[\frac{H_{lp}(s - jk\omega_0)(R_k - jI_k)}{s - jk\omega_0} + \frac{H_{lp}(s + jk\omega_0)(R_k + jI_k)}{s + jk\omega_0}\right], \quad k = 1, \ldots, n_h \tag{4}$$

in which $g_{p,k}$ is an adjustable scalar gain that controls the time constant of the kth frequency channel. Poles at $\pm jk\omega_0$ provide asymptotic tracking of a periodic signal at $k\omega_0$. An additional analysis of the dynamics of the inner loop from both the measurement and baseband perspectives is given in [18,22].

Measurement of the inner-loop complementary sensitivity function (Fig. 9, top plot) demonstrates that asymptotic tracking is achieved at the 20 harmonics of 100 Hz targeted for control. The phase is not shown; however, the phases at the frequencies $k\omega_0$, $k = 1, \ldots, 20$, are zero. The data are produced using broadband white noise injected at u_{test} in Fig. 7, with the test-input amplitude adjusted to perturb the jet velocity by 0.15 ms^{-1} rms ($\tilde{r}_p = 0$). In addition to the pressure measurement, the velocity measurement is recorded and used to calculate the transfer function from u_{test} to y_v (Fig. 9, bottom plot). The pressure loop's equalizing effect on the jet-velocity magnitude is evident by the similar magnitude responses at each frequency of control. Additionally, although the velocity-perturbation amplitude is small, the nonlinear effects of the velocity system appear in the transfer function at harmonics of 100 Hz that fall beyond 2 kHz. These peaks result from nonlinear harmonic coupling, and grow stronger with increased forcing amplitude.

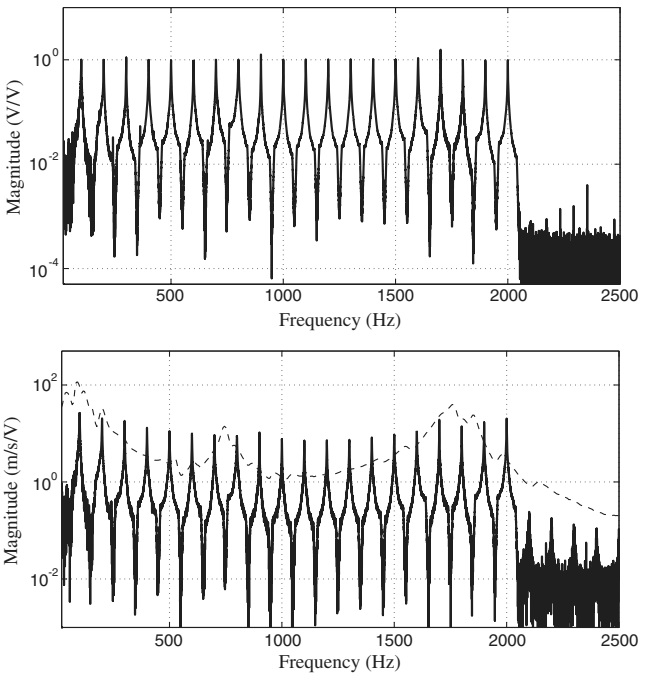

Fig. 9 Complementary sensitivity function of the pressure inner loop (top) and transfer function from r_p to y_v (bottom).

C. Harmonic-Coupling-Identification Results

The coupling between channels in $\tilde{P}_v$ is a function of the operating point, and so it is necessary to specify a constant pressure-reference vector $\bar{r}_p$ such that the elements of $\tilde{y}_v$ are close to the values associated with the Fourier series of the desired periodic jet-velocity waveform. The coupling is identified at the operating condition by adding a time-varying perturbation to the constant reference. In other words, the reference input in Fig. 7 is specified to be $\tilde{r}_p = \bar{r}_p + \delta_p$, in which δ_p is the perturbation employed for identification in a neighborhood of the operating condition established by $\bar{r}_p$. The appropriate values for $\bar{r}_p$ must be specified though. Let the desired periodic jet-velocity waveform y_{ref} with fundamental frequency ω_0 possess the following Fourier series:

$$\frac{\omega_0}{2\pi}\sum_{k=0}^{\infty} a_k \cos(k\omega_0 t) + b_k \sin(k\omega_0 t), \qquad a_k + jb_k = \int_0^{\frac{2\pi}{\omega_0}} y_{\text{ref}}(t)e^{-jk\omega_0 t}\,dt \tag{5}$$

The constant reference vector $\bar{r}_p$ should be chosen, so that $\bar{y}_v$ satisfies

$$[\bar{y}^i_{v,1}, \quad \bar{y}^q_{v,1}, \quad \bar{y}^i_{v,2}, \quad \ldots, \quad \bar{y}^i_{v,n_h}, \quad \bar{y}^q_{v,n_h}] = [a_1, b_1, a_2, \ldots, a_{n_h}, b_{n_h}] \tag{6}$$

If we treat P_v as a linear system with frequency-response function $P_v(j\omega)$, then the in-phase and quadrature components of $\bar{r}_p$ associated with the kth frequency would be chosen such that

$$\bar{r}^i_{p,k} + j\bar{r}^q_{p,k} = P_p(jk\omega_0)P_v^{-1}(jk\omega_0)(a_k + jb_k), \qquad k = 1, \ldots, n_h \tag{7}$$

In practice, the values of $P_v(jk\omega_0)$ are selected based on the linear jet-velocity model from Fig. 2. This method does not compensate for the nonlinear dynamics of P_v or for identification errors in P_p, and as a consequence equality in Eq. (6) does not hold and y_v does not track y_{ref}. The outer loop using the velocity measurement for feedback, however, will use the right-hand side of Eq. (6) as the reference input $\bar{r}_v$. Some examples of the jet-velocity waveform when $\bar{r}_p$ is chosen in this manner are shown in Fig. 10, in which the measured jet-velocity waveforms (solid lines) are compared to their respective reference waveforms (dashed lines). The references are 20% duty-cycle tapered square pulses with amplitudes ranging from $V_{\text{rms}} = 0.3$ ms^{-1} to $V_{\text{rms}} = 1.2$ ms^{-1}. The asymmetry and oscillation seen in the empirical waveform grow with amplitude due to increased harmonic coupling at higher rms forcing amplitudes. While these waveforms do not match the desired periodic waveform, they are adequate to identify a model of the harmonic coupling in a neighborhood of the operating point, which is then employed to design the stabilizing outer loop.

The small signal behavior of the jet velocity in a neighborhood of the operating point will be modeled as a linear time-invariant system. In response to the pressure reference $\tilde{r}_p = \bar{r}_p + \delta_p$, in which $\bar{r}_p$ establishes the jet-velocity operating point $\bar{y}_v$, the demodulated velocity components are $\tilde{y}_v = \bar{y}_v + \delta_v$, in which δ_v is the time-varying portion of $\tilde{y}_v$. For a sufficiently small δ_p, we model $\delta_v = h * \delta_p$, in which h is a $2n_h$-input/$2n_h$-output linear system, and

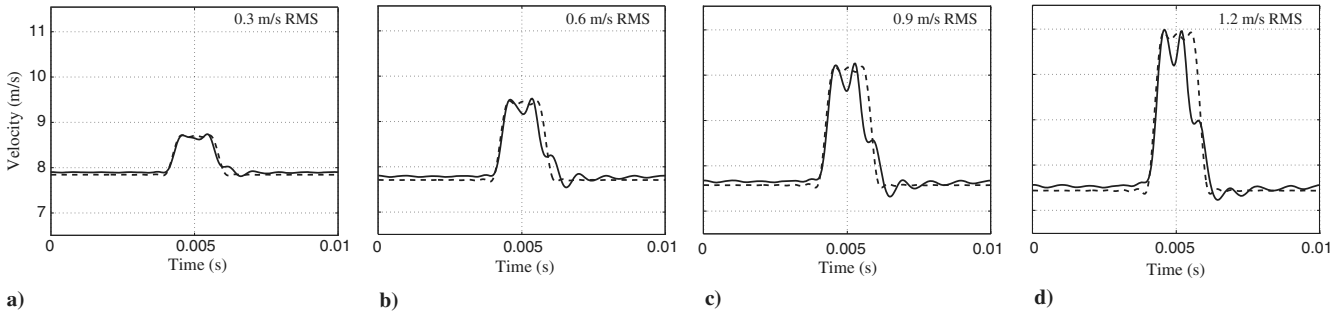

Fig. 10 Operating points established for identication (solid) compared to the jet velocity reference (dash) at a) $V_{\text{rms}} = 0.3$ ms^{-1} b) $V_{\text{rms}} = 0.6$ ms^{-1} c) $V_{\text{rms}} = 0.9$ ms^{-1} and d) $V_{\text{rms}} = 1.2$ ms^{-1}.

$*$ is the convolution operator. Note that h is a function of the operating point established by $\bar{r}_p$, but this dependency is suppressed for the sake of streamlined notation. The elements of the perturbation variables follow the conventions established for $\tilde{r}_p$ and $\tilde{y}_p$, namely

$$\delta_p = [\,\delta^i_{p,1},\quad \delta^q_{p,1},\quad \delta^i_{p,2},\quad \ldots,\quad \delta^i_{p,n_h},\quad \delta^q_{p,n_h}\,]^T$$
$$\delta_v = [\,\delta^i_{v,1},\quad \delta^q_{v,1},\quad \delta^i_{v,2},\quad \ldots,\quad \delta^i_{v,n_h},\quad \delta^q_{v,n_h}\,]^T$$

Although the model is developed about a periodic operating point, in the demodulated signal space, the periodicity is manifested by constant signal values so that h can be treated as a time-invariant system, too. We consider in detail a few channels of h in a neighborhood of two operating points.

An empirical frequency response associated with the lth input channel to the kth output channel of h is identified by adding low-bandwidth zero-mean random perturbations to the constant in-phase term $\bar{r}_{p,l}$. The low-bandwidth random input signal represents $\delta^i_{p,l}$. The in-phase and quadrature responses to this input are measured for the kth output channel, and the mean values are removed to yield the signals $\delta^i_{v,k}$ and $\delta^q_{v,k}$. The experiment is repeated, but now using the quadrature input $\delta^q_{p,l}$. A traditional cross-spectral estimation is employed to develop empirical frequency responses between these input and output pairs. For example, Fig. 11 presents the frequency-response estimates from in-phase inputs $\delta^i_{p,15}$ and $\delta^i_{p,16}$ to outputs $\delta^i_{v,15}$, $\delta^q_{v,15}$, $\delta^i_{v,16}$, $\delta^q_{v,16}$ $\delta^i_{v,17}$, and $\delta^q_{v,17}$ at the unforced operating point $V_{\text{rms}} = 0.0$ ms^{-1}. Figure 12 shows the frequency-response estimates using the channels 15 and 16 quadrature inputs to the same output variables. These figures demonstrate how perturbations to the 15th and 16th channels (corresponding to frequency bins centered at 1.5 and 1.6 kHz) couple to signals in the 15th, 16th, and 17th channels (corresponding to frequency bins centered at 1.5, 1.6, and 1.7 kHz). Note that the off-diagonal transfer functions can be modeled as zero. Further testing of all channels leads to the conclusion that all off-diagonal channels are zero when $V_{\text{rms}} = 0$ ms^{-1} (i.e., $\delta^i_{v,k}/\delta^q_{p,l} = 0$ when $k \neq l$).

In marked contrast is the system behavior in the presence of periodic forcing at a 20% duty cycle with $V_{\text{rms}} = 0.9$ ms^{-1} (corresponding to the operating point in Fig. 10c) shown in Figs. 13 and 14. These figures demonstrate that not only have the diagonal frequency responses changed from the $V_{\text{rms}} = 0$ ms^{-1} case, but that the off-diagonal magnitudes are now nonzero, and in some cases, are as large as the diagonal magnitudes. This cross-channel coupling clearly reveals the nonlinear behavior of the jet velocity. The figures also reveal additional structure in h. Comparing Fig. 11 to 12, and Fig. 13 to 14, it is evident that, for a given channel, the in-phase-to-in-phase frequency response is close in magnitude and phase to the quadrature-to-quadrature frequency response. Furthermore, the cross-element magnitudes are similar, and the phases differ by about 180 deg. Despite the differences (some of which can be attributed to slow drift of the test conditions primarily caused by changes in the mean jet velocity), we will assume for the purpose of identification:

$$\begin{aligned}\delta^i_{v,k}/\delta^i_{p,l} &= \delta^q_{v,k}/\delta^q_{p,l}\\ \delta^i_{v,k}/\delta^q_{p,l} &= -\delta^q_{v,k}/\delta^i_{p,l}\end{aligned}\quad l,k = 1,\ \ldots,\ n_h \tag{8}$$

This structure can be proven for the diagonal blocks of a linear system such as the demodulated model associated with P_p; however, for a nonlinear system such as P_v, we currently have no general proof that its demodulated model should possess this structure. Nevertheless, the experimental data (including the other channels not shown here) support the assumption (8).

The high channel count associated with the linearizations requires an efficient method for determining a suitable model for controller design. It is much too labor intensive to perform the sort of experiments that produce the frequency-response estimates of Figs. 11–14, and, in fact, such detailed models are not necessary for controller synthesis. Let $H(s)$ represent the Laplace transform of h. We will show that the dc gain of the frequency response, in other words, $H(0)$, is adequate for the successful synthesis of low-bandwidth jet-velocity compensators. In other words, at a given operating point, we identify a model of the form

$$\delta_v(t) = H(0)\delta_p(t) \tag{9}$$

in which $H(0) \in \mathbb{R}^{2n_h \times 2n_h}$ is the dc-gain matrix to be determined. Because of the assumed structure of h though, only n_h inputs are required to identify $H(0)$, and so the quadrature components of δ_p are held at zero while the in-phase components are (simultaneously) specified to be low-bandwidth (0.2 Hz) uncorrelated random zero-mean sequences. The new vector $\delta^i_p(t) \in \mathbb{R}^{n_h}$ is obtained from δ_p by eliminating the quadrature components. The input–output data are collected and assembled as follows:

$$\Delta_v = \{\,\delta_v(0)\quad \delta_v(t_s)\quad \delta_v(2t_s)\quad \ldots\quad \delta_v[(n_e-1)t_s]\,\} \in \mathbb{R}^{2n_h \times n_e}$$
$$\Delta_p = \{\,\delta^i_p(0)\quad \delta^i_p(t_s)\quad \delta^i_p(2t_s)\quad \ldots\quad \delta^i_p[(n_e-1)t_s]\,\} \in \mathbb{R}^{n_h \times n_e}$$

in which $\delta_v(kt_s)$ and $\delta^i_p(kt_s)$ are the output and input data at time $t = kt_s$, $k = 0, 1, \ldots, n_e - 1$, and in which n_e is the number of collected time samples. The matrix $\tilde{H} \in \mathbb{R}^{2n_h \times n_h}$ is obtained from $H(0)$ by deleting the columns corresponding to the quadrature inputs. Once $\tilde{H}$ is determined though, $H(0)$ can be constructed from Eq. (8). A standard least-squares problem is solved to minimize the norm of the prediction error:

$$\tilde{H}_{\text{ls}} = \arg\min_{\tilde{H}} \bar{\sigma}(\Delta_v - \tilde{H}\Delta_p) \tag{10}$$

The uncorrelated inputs ensure that Δ_p is full rank, and so a unique minimizing solution exists.

The quality of the fit can be quantified by comparing Δ_v obtained from another data set to what is predicted using the least-squares solution $\tilde{H}_{\text{ls}}\Delta_p$. For example, when $V_{\text{rms}} = 0.9$ ms^{-1} with a 20% duty cycle, the normalized prediction error on a new data set is $\bar{\sigma}(\Delta_v - \tilde{H}_{\text{ls}}\Delta_p)/\bar{\sigma}(\Delta_v) \approx 0.2$. Time sequences can also be compared, and Fig. 15 shows the measured and predicted in-phase and quadrature velocity signals for the 15th, 16th, and 17th output channels. The prediction error is small, and $H(0)$ accurately captures the low-frequency linearized dynamics of the harmonic coupling. Thus, this technique is used to rapidly determine the low-frequency system dynamics at all operating points.

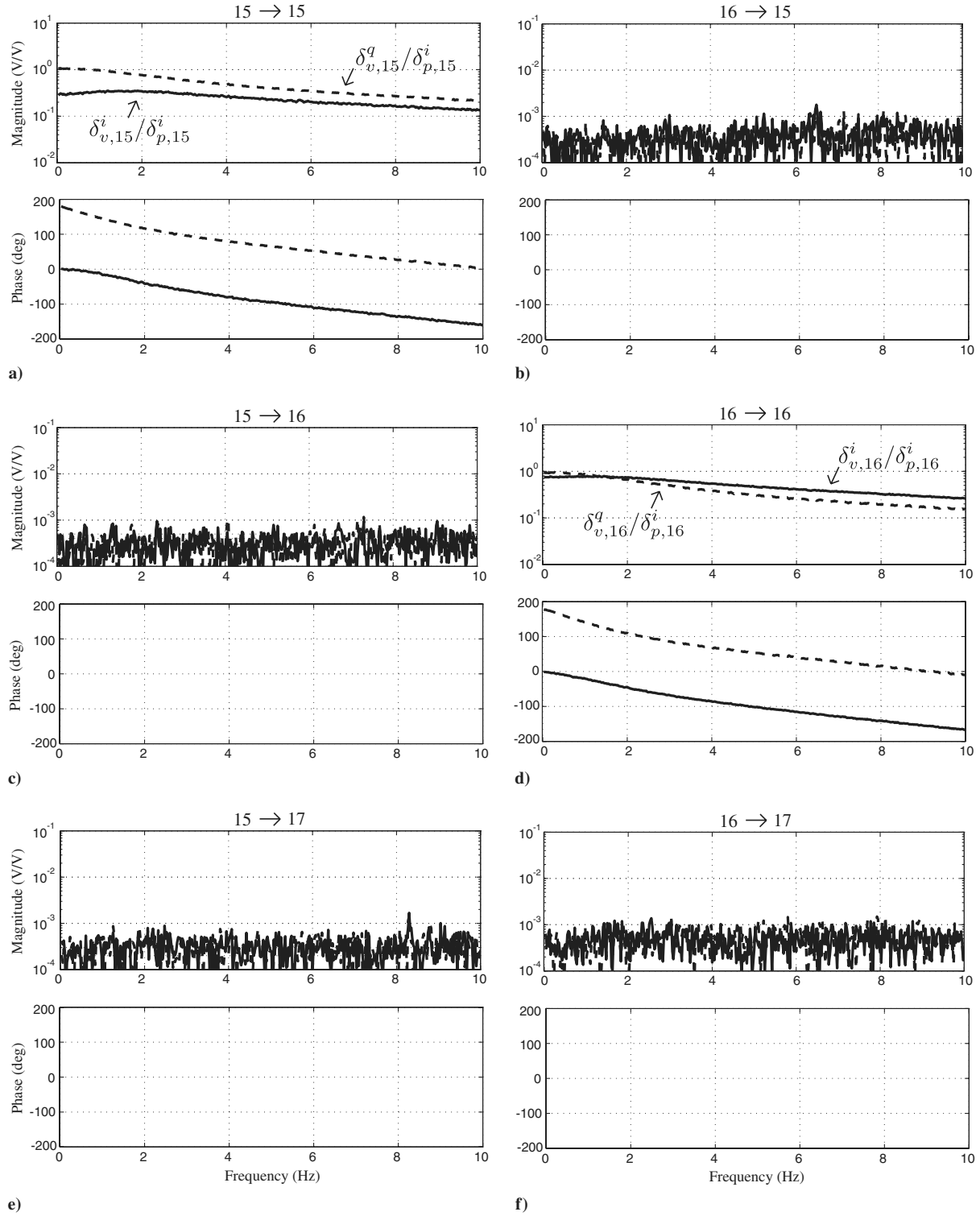

Fig. 11 System identification at the unforced operating point using in-phase inputs yields the frequency responses a) $\delta^i_{v,15}/\delta^i_{p,15}$ and $\delta^q_{v,15}/\delta^i_{p,15}$, b) $\delta^i_{v,15}/\delta^i_{p,16}$ and $\delta^q_{v,15}/\delta^i_{p,16}$, c) $\delta^i_{v,16}/\delta^i_{p,15}$ and $\delta^q_{v,16}/\delta^i_{p,15}$, d) $\delta^i_{v,16}/\delta^i_{p,16}$ and $\delta^q_{v,16}/\delta^i_{p,16}$, e) $\delta^i_{v,17}/\delta^i_{p,15}$ and $\delta^q_{v,17}/\delta^i_{p,15}$, and f) $\delta^i_{v,17}/\delta^i_{p,16}$ and $\delta^q_{v,17}/\delta^i_{p,16}$.

A graphical representation of $H(0)$ is also possible and is useful for viewing changes in $H(0)$ as the operating point is modified. Because there are 20 frequency bins associated with the demodulated input and output signals, the norm of a given channel can be represented as a grayscale shade in a figure with 20×20 cells. The norm of the lth input channel to the kth output channel is

$$\bar{\sigma}\left(\begin{bmatrix} \delta^i_{v,k}/\delta^i_{v,l} & \delta^i_{v,k}/\delta^q_{v,l} \\ -\delta^i_{v,k}/\delta^q_{v,l} & \delta^i_{v,k}/\delta^i_{v,l} \end{bmatrix}\right) = \sqrt{(\delta^i_{v,k}/\delta^i_{v,l})^2 + (\delta^i_{v,k}/\delta^q_{v,l})^2}$$

in which only the dc values of the transfer functions are used in the calculation. Figure 16 provides three such graphical representations: one at the unforced operating point (Fig. 16a); another at the 20% duty cycle, $V_{\text{rms}} = 0.45$ ms^{-1} operating point (Fig. 16b); and the third at the 20% duty cycle, $V_{\text{rms}} = 0.9$ ms^{-1} operating point (Fig. 16c). At the unforced operating point, $H(0)$ is essentially block diagonal, which indicates little-to-no harmonic coupling. At higher forcing amplitudes, however, the figures reveal strong harmonic coupling, especially between frequencies above 800 Hz.

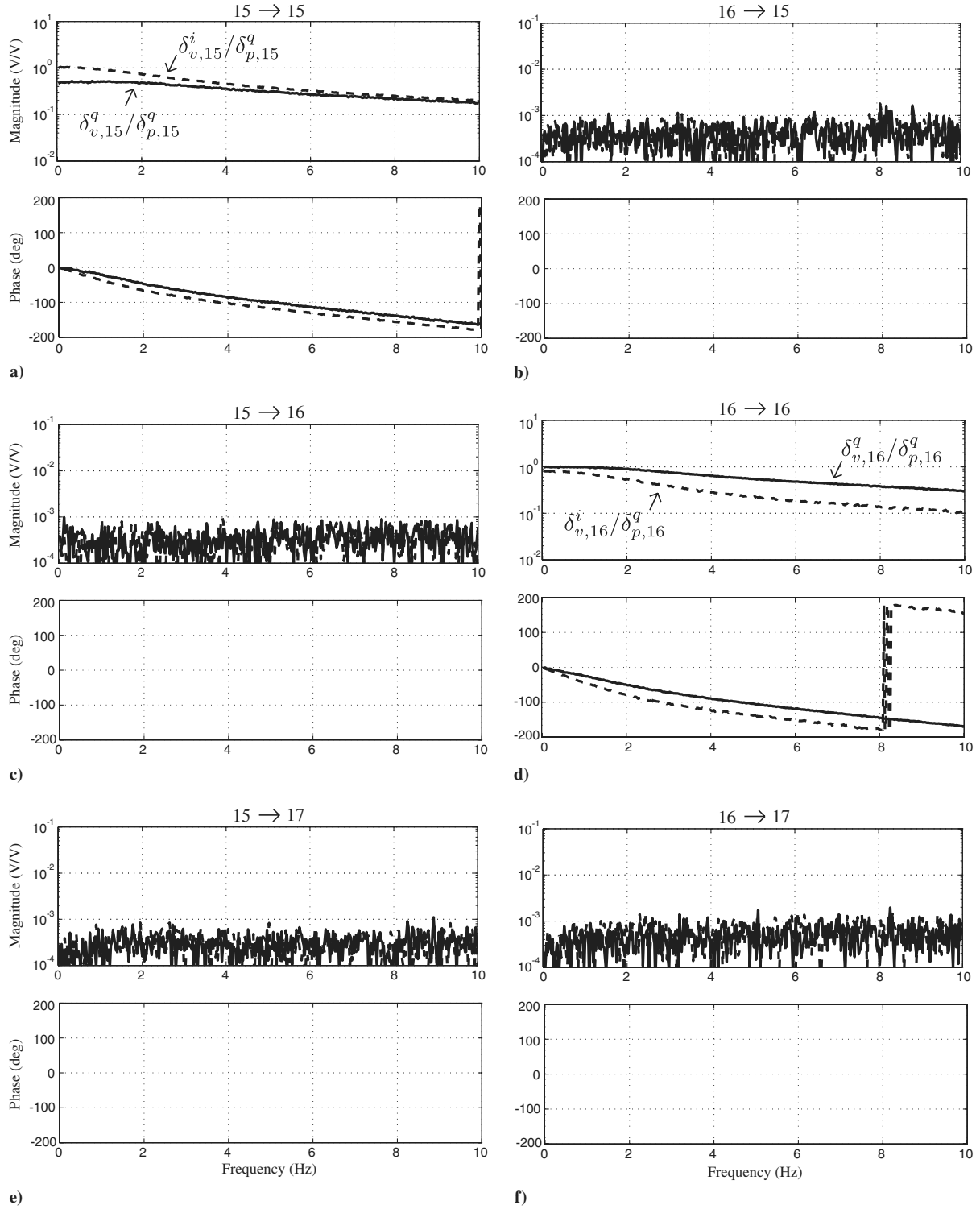

Fig. 12 System identification at the unforced operating point using quadrature inputs yields the frequency responses a) $\delta^i_{v,15}/\delta^q_{p,15}$ and $\delta^q_{v,15}/\delta^q_{p,15}$, b) $\delta^i_{v,15}/\delta^q_{p,16}$ and $\delta^q_{v,15}/\delta^q_{p,16}$, c) $\delta^i_{v,16}/\delta^q_{p,15}$ and $\delta^q_{v,16}/\delta^q_{p,15}$, d) $\delta^i_{v,16}/\delta^q_{p,16}$ and $\delta^q_{v,16}/\delta^q_{p,16}$, e) $\delta^i_{v,17}/\delta^q_{p,15}$ and $\delta^q_{v,17}/\delta^q_{p,15}$, and f) $\delta^i_{v,17}/\delta^q_{p,16}$ and $\delta^q_{v,17}/\delta^q_{p,16}$.

IV. Compensation of Harmonic Coupling

Two compensation strategies are implemented for the asymptotic tracking of the periodic jet-velocity-reference waveform within the system's 2 kHz bandwidth: regulation about a single operating point and regulation about multiple operating points with a single controller. In both cases, the demodulated hot-wire signal $\tilde{y}_v$ is subtracted from the constant reference $\bar{r}_v$, which contains the Fourier coefficients of the reference waveform. The resulting tracking error drives the velocity controller $\tilde{C}_v$, as shown in the block diagram of Fig. 17. The reference for the velocity control loop is

$$\bar{r}_v = [\,a_1, \quad b_1, \quad a_2, \quad \ldots, \quad a_{n_h}, \quad b_{n_h}\,]^T$$

in which the elements are the Fourier coefficients from Eq. (5). The objective of this section is not to present an exhaustive investigation into the various synthesis methods that can be applied to this problem, but to demonstrate that the linearized models

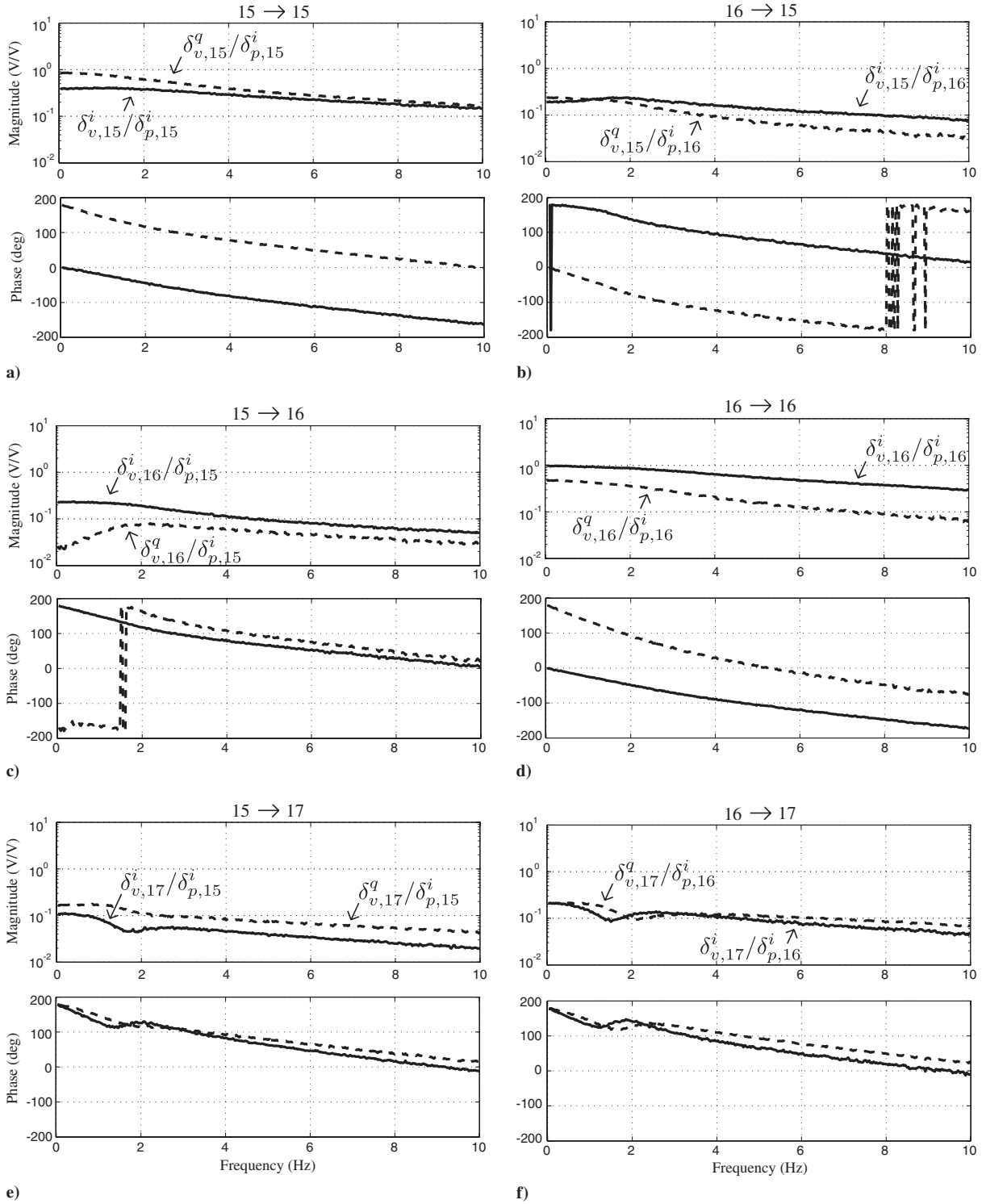

Fig. 13 Same as Fig. 11, but the operating point is now a 20% duty cycle square wave with $V_{\text{rms}} = 0.9$ ms^{-1}.

created from the demodulated variables are quite useful for understanding and compensating the strongly nonlinear behavior of the jet. We focus on the case of the 20% duty cycle forcing with $\omega_0 = 100$ Hz and desired forcing strengths ranging from $V_{\text{rms}} = 0$ ms^{-1} to 1.05 ms^{-2}.

A. Regulation at a Single Operating Point

Stabilization is rarely the sole objective of feedback control; however, in this application, we are interested in a controller that can generate a suitable low-frequency plant inverse so that the desired periodic jet-velocity waveform is asymptotically tracked. With the pressure reference $\bar{r}_p$ in Fig. 17 establishing a periodic jet velocity close to the desired waveform, the controller is required to issue perturbations to the reference values such that the demodulated jet-velocity components asymptotically converge to $\bar{r}_v$. This suggests the use of integral control in all channels to asymptotically drive the tracking error $\tilde{e}_v$ to zero:

$$\tilde{C}_v(s) = g_v K_v \frac{1}{s} \tag{11}$$

in which $K_v \in \mathbb{R}^{2n_h \times 2n_h}$ is a constant real matrix, and g_v is a real positive scalar gain that sets the outer-loop convergence rate. The continuous-time controller realization is

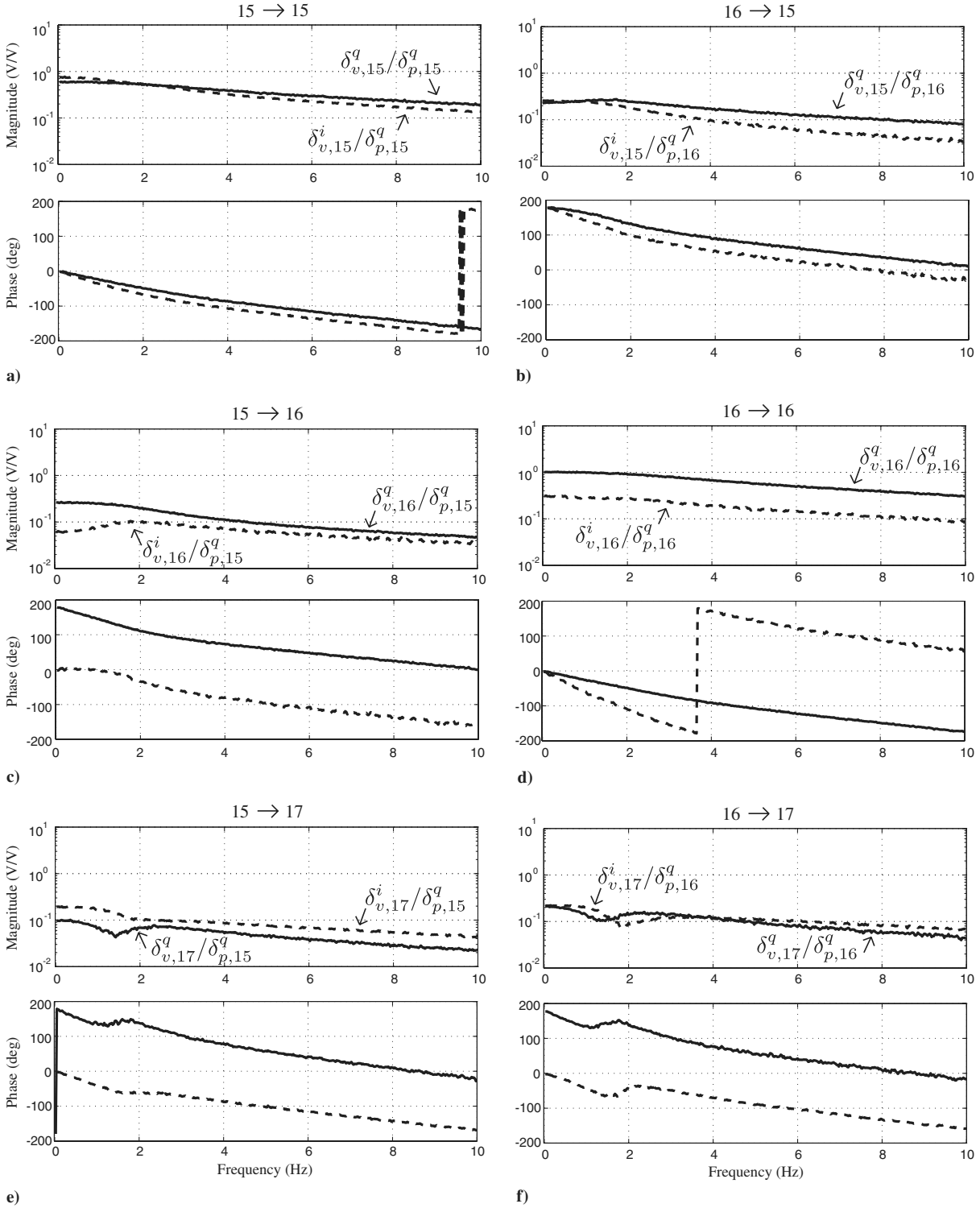

Fig. 14 Same as Fig. 12, but the operating point is now a 20% duty cycle square wave with $V_{\text{rms}} = 0.9$ ms^{-1}.

$$\dot{\mathbf{x}}_v = \tilde{e}_v, \qquad \delta_p = K_v \mathbf{x}_v \tag{12}$$

in which $\mathbf{x}_v(t) \in \mathbb{R}^{2n_h}$ is the controller state. The closed-loop system with the simplified plant model is simply $\dot{\mathbf{x}}_v = -g_v H(0) K_v \mathbf{x}_v$. Because the velocity control loop is implemented at a 2.5 kHz sample rate (the microphone and hot-wire signals are sampled at 25 kHz, demodulated, and then downsampled to 2.5 kHz), the computational power of the computer enables the use of a fully populated K_v, in which every element may be nonzero. Thus, K_v is chosen as the inverse of $H(0)$ identified in Sec. III.C [i.e., $K_v = H^{-1}(0)$]. This approach yields a robust closed-loop system because the condition number of $H(0)$ is relatively low at all operating points due to the equalizing effect of the inner feedback loop illustrated in Fig. 9 (see [24]). The equalizing effect lowers the condition number κ of $H(0)$ at the unforced operating point to $\kappa[H(0)] = 2.7$ from its open-loop value of $\kappa = 706$. At higher forcing amplitudes, the harmonic coupling increases the condition number. For example, at $V_{\text{rms}} = 0.45$ ms^{-1}, the condition number of $H(0)$ is $\kappa = 4.0$, and at $V_{\text{rms}} = 0.9$ ms^{-1}, the condition number increases to $\kappa = 8.3$. In all cases, however, the inverse of the plant's dc-gain matrix can be safely used. All (continuous-time) closed-loop eigenvalues are located at $-g_v$, in which g_v is selected so that the closed-loop time constant is 1 s.

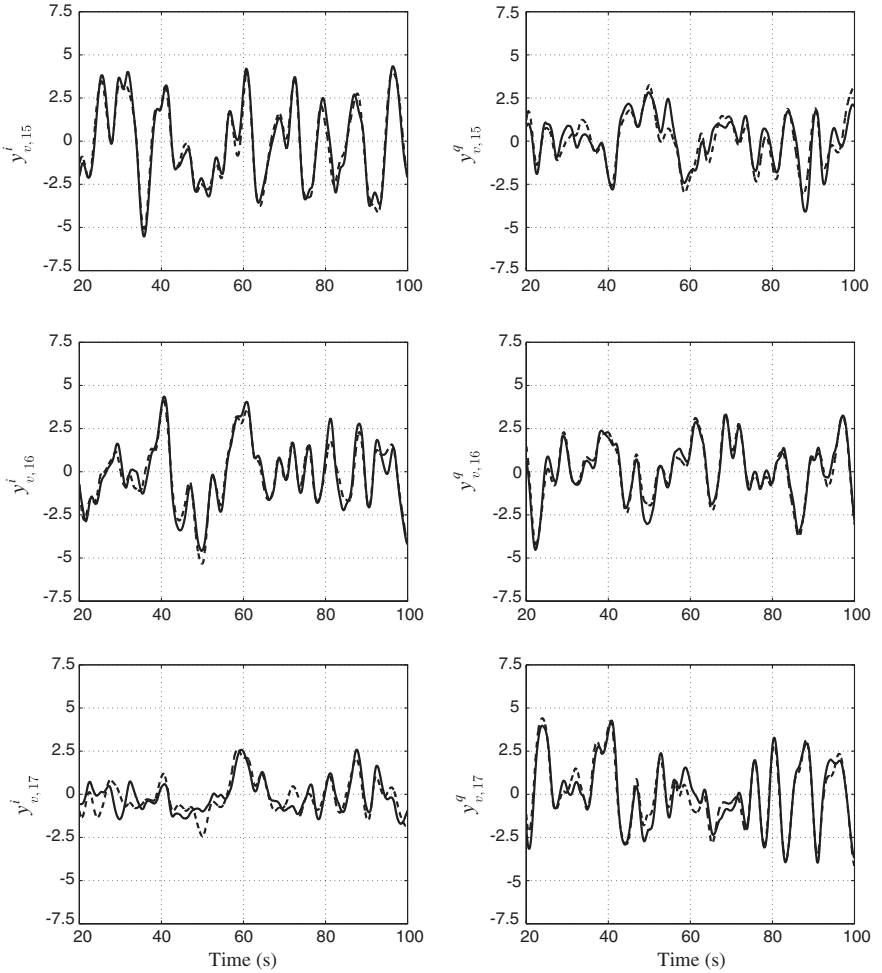

Fig. 15 Response of the demodulated hot-wire signal $\tilde{y}_v$ (solid) compared to the model prediction (dash).

There is one technical detail to be addressed, and that is to show there is no possibility of cancellation between a controller pole at $s = 0$ with a transmission zero of $H(s)$. This is easily demonstrated by assuming a minimal realization for H to be $\dot{\mathbf{x}} = A\mathbf{x} + B\delta_p$, $\delta_v = C\mathbf{x}$ in which $\mathbf{x}(t) \in \mathbb{R}^m$, m is the state dimension of H, $A \in \mathbb{R}^{m\times m}$, $B \in \mathbb{R}^{m\times 2n_h}$, and $C \in \mathbb{R}^{2n_h\times m}$. We may assume H is strictly proper because H_{lp} rolls off all channels. Transmission zeros at $s = 0$ require det $Q = 0$, in which Q is defined as

$$\begin{bmatrix} -A & -B \\ C & 0 \end{bmatrix} \in \mathbb{R}^{(m+2n_h)\times(m+2n_h)}$$

and in which 0 denotes a $2n_h \times 2n_h$ matrix of zeros [25]. The asymptotic stability of H means det $A \neq 0$, and so det $Q =$ det A det$(CA^{-1}B)$. Note though, $H(0) = -CA^{-1}B$ is invertible, and it follows that det $Q \neq 0$ so that H cannot have transmission zeros at $s = 0$. The implication is that the controller $\tilde{C}_v = g_v H^{-1}(0)(1/s)$ internally stabilizes the plant $H(s)$ if g_v is sufficiently small.

The steady-state closed-loop jet-velocity waveforms with the outer-loop controller designed according to this prescription are shown in Fig. 18. In all four cases, the velocity-loop controllers asymptotically drive the demodulated hot-wire signals to the Fourier coefficients of the reference waveforms at the 20 frequencies of control. The measured jet-velocity waveforms (solid lines) closely match the references (dashed lines). Note that the jet-velocity references are identical to those in Fig. 10 for pressure-only feedback. At each reference amplitude, a unique $\tilde{C}_v$ is synthesized using $H(0)$ identified at the operating points shown in Fig. 10. The spectra of the $V_{\text{rms}} = 0.9$ ms^{-1} jet-velocity waveform, y_v, and the reference coefficients, $\bar{r}_v$ (expressed in polar form), shown in Fig. 19, verify that the Fourier coefficients of y_v match the reference coefficients at all frequencies of control. Small periodic errors are evident in the high-amplitude time series, and are the result of harmonics excited beyond 2.0 kHz. As these harmonics lie beyond the bandwidth of the actuation system, they are uncompensated.

The controllers effectively regulate the jet velocity in a neighborhood of an operating point; however, instability may occur if the velocity reference $\bar{r}_v$ moves sufficiently far from the operating point about which the controller design was based. For example, a 20% duty-cycle square wave is tracked using the controller synthesized from the identification of $H(0)$ at the unforced operating point (Fig. 16a). With the outer loop closed, the velocity reference is increased from zero until instability occurs. Note that increasing the pulse height with fixed duty cycle (as is done here) just requires a real scaling of $\bar{r}_v$. Figure 20 shows the norm of the velocity-loop tracking error $\|\tilde{e}_v(t)\|_2 = \|\bar{r}_v - \tilde{y}_v(t)\|_2$ as the jet-velocity rms amplitude is increased from 0 to 0.6 ms^{-1} in steps of 0.15 ms^{-1}, occurring every 30 s. The error is regulated to zero after each step until $t = 120$ s, in which, at $V_{\text{rms}} = 0.6$ ms^{-1}, the closed-loop system is unstable. The instability can be predicted by analyzing the eigenvalues λ_{cl} of $-g_v H(0)K_v$, in which K_v is based on the identification at $V_{\text{rms}} = 0$ ms^{-1}, and $H(0)$ is changed according to the V_{rms} implied by the velocity reference. Table 1 lists the predicted maximum real part of λ_{cl} for the four V_{rms} cases, and shows that instability occurs somewhere between $V_{\text{rms}} = 0.45$ ms^{-1} and $V_{\text{rms}} = 0.6$ ms^{-1} as is experimentally observed ($g_v = 1$ in this experiment).

B. Regulation at Multiple Operating Points

It may be possible to synthesize a single controller that stabilizes the system at multiple operating conditions. The previous section demonstrated that a controller designed at a given operating point may, indeed, also stabilize the closed-loop system at other operating

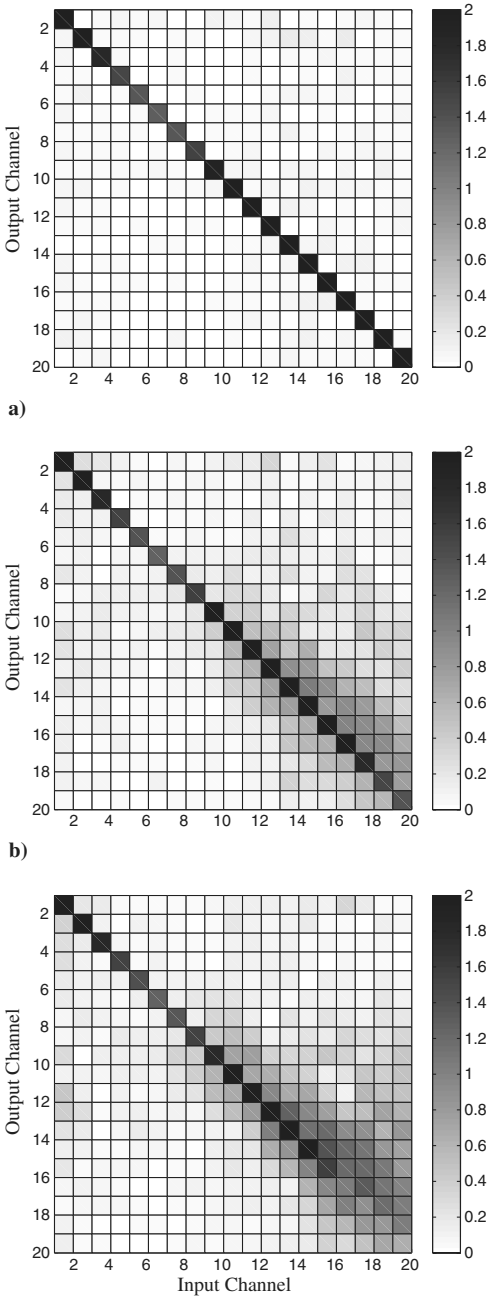

Fig. 16 Graphical representation of $H(0)$.

points; however, the objective of this section is to show that, if multiple operating points are a priori considered in the controller design, a larger range of operating conditions can be stabilized with a single controller. A single controller is desired for ease of implementation. The controller remains an integrator for which the gain matrix K_v is to be designed. The synthesis problem is established by considering the backward-difference discrete-time approximation of Eq. (12):

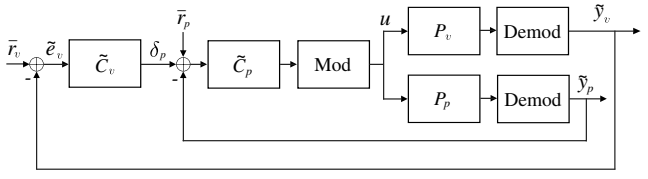

Fig. 17 Compensation of harmonic coupling using outer-loop feedback of the jet velocity.

$$\mathbf{x}_v((k+1)t_s) = \mathbf{x}_v(kt_s) + t_s\tilde{e}_v(kt_s), \qquad \delta_p(kt_s) = K_v\mathbf{x}_v(kt_s)$$

in which t_s is the sample period, k is an integer denoting the sample index, and $g_v = 1$. The closed-loop system at an operating point with dc gain $H(0)$ is

$$\mathbf{x}_v((k+1)t_s) = (I - t_sH(0)K_v)\mathbf{x}_v(kt_s)$$

A sufficient condition for closed-loop asymptotic stability is $\bar{\sigma}(I - t_sH(0)K_v) < 1$, and so if there are n_p operating points with dc-gain matrices $H_k(0)$, $k = 1, \ldots, n_p$, then a search can be performed for a single K_v such that $\bar{\sigma}(I - t_sH_k(0)K_v) < 1$, $k = 1, \ldots, n_p$. The synthesis of K_v can be (conservatively) formulated as

$$\min_{K_v} \max_k \bar{\sigma}(I - t_sH_k(0)K_v)$$

which can be expressed as a generalized-eigenvalue-minimization problem

$$\begin{aligned} &\text{minimize} && \gamma \\ &\text{subject to} && 0 < \Sigma(K_v) \\ &&& \beta_k < \gamma I, k = 1, \ldots, n_p \end{aligned} \tag{13}$$

The matrix $\Sigma(K_v)$ is defined

$$\Sigma(K_v) = \begin{bmatrix} \alpha I & K_v \\ K_v^T & \alpha I \end{bmatrix} \tag{14}$$

in which α is a positive real constant that enforces $\bar{\sigma}(K_v) < \alpha$. The matrices β_k are defined

$$\beta_k = \begin{bmatrix} 0 & I - t_sH_k(0)K_v \\ (I - t_sH_k(0)K_v)^T & 0 \end{bmatrix}, \qquad k = 1, \ldots, n_p \tag{15}$$

Setting $\gamma > 1$ and $K_v = 0$ yields a feasible starting point, and, if in the course of the optimization $\gamma < 1$, the associated K_v asymptotically stabilizes the system at all n_p operating points. With multiple operating points though, there is no guarantee of finding a single stabilizing gain K_v. In fact, it is straightforward to construct examples for which there does not exist a stabilizing solution. Furthermore, the conservatism introduced by using $\bar{\sigma}$ means that, even if a stabilizing solution exists, it does not imply $\gamma^* < 1$. Nevertheless, this approach has been useful in generating controllers that successfully stabilize a range of operating points that cannot be stabilized by a controller designed for a single operating point. The closed-loop convergence rate cannot be specified with this approach; however, if $\gamma^* < 1$, then the closed-loop time constant is no larger than $-t_s/\log\gamma^*$. If the adjustable gain parameter g_v is introduced in the controller, then the eigenvalues of $I - g_vt_sH_k(0)K_v$ are affine functions of g_v, and all closed-loop eigenvalues converge to 1 as $g_v \to 0$. Thus, if the eigenvalues of $I - t_sH_k(0)K_v$ are stable, then so are the eigenvalues of $I - g_vt_sH_k(0)K_v$ for $g_v \in (0, 1]$; this provides a means of adjusting the convergence rate. The bound on the maximum singular value of the controller gain α is often an inactive constraint in the optimization; however, it can be included to limit the maximum controller gain.

This synthesis approach is used to generate a single controller that can track a 20% duty-cycle square wave over a wide amplitude range. The optimization is executed with $\alpha = 5$, and a set of $n_p = 4$ gain matrices identified at $V_{\text{rms}} = \{0, 0.6, 0.9, 1.05\}$ ms^{-1} operating points. MATLAB's linear-matrix-inequality solvers were used to generate solutions to Eq. (13) [26]. The optimization yields a controller that stabilizes all operating points, and $\gamma^* = 0.999982$ guarantees time constants smaller than 20 s ($t_s = 0.0004$). The range of amplitudes stabilized with this controller is more than double the range stabilized with the $V_{\text{rms}} = 0$ ms^{-1} model inverse controller presented in Fig. 20. Figure 21 shows $\|\tilde{e}_v\|_2$ as the reference amplitude is stepped from $V_{\text{rms}} = 0$ to 1.05 ms^{-1}. The amplitude is

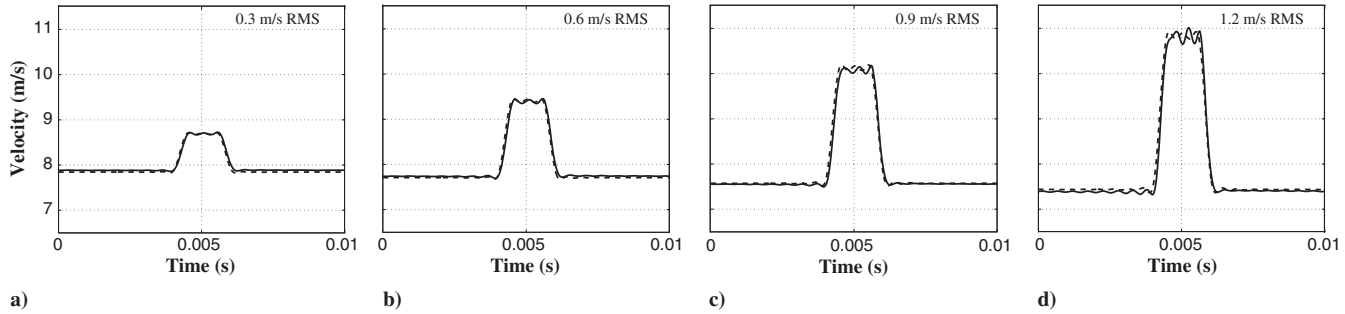

Fig. 18 Jet velocity (solid) with velocity and pressure feedback compared to the velocity reference (dash) at a) $V_{\text{rms}} = 0.3$ ms^{-1} b) $V_{\text{rms}} = 0.6$ ms^{-1} c) $V_{\text{rms}} = 0.9$ ms^{-1}, and d) $V_{\text{rms}} = 1.2$ ms^{-1}.

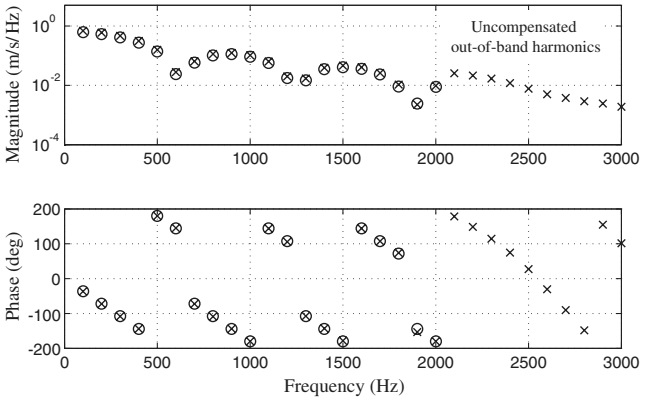

Fig. 19 Spectra of y_v (×) and y_{ref} (○) for the $V_{\text{rms}} = 0.9$ ms^{-1} case in Fig. 18c.

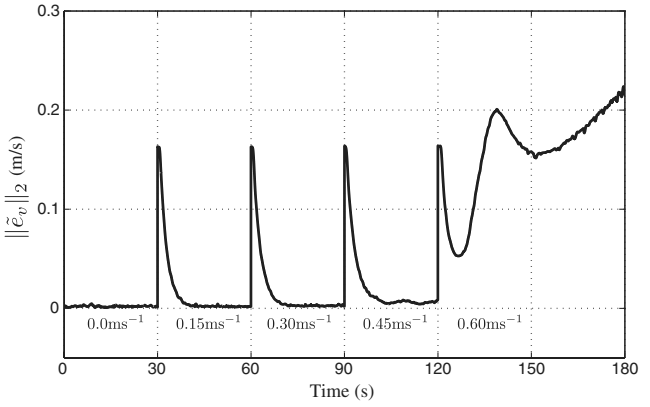

Fig. 20 Error-signal norm, $\|\tilde{e}_v\|_2$, using the $V_{\text{rms}} = 0$ ms^{-1} model inverse controller.

incrementally increased in steps of 0.15 ms^{-1} every 20 s, and the error asymptotically converges to zero after every step change in amplitude. Increasing V_{rms} beyond 1.05 ms^{-1} is not possible due to saturation of the amplifier input. Note that the closed-loop time constants are considerably smaller than the upper bound derived from γ^*.

Table 1 Predicted maximum closed-loop eigenvalue

V_{rms}, ms^{-1}	Max[real(λ_{cl})]
0.00	−1.00
0.15	–0.93
0.30	−0.69
0.45	−0.16
0.60	0.39

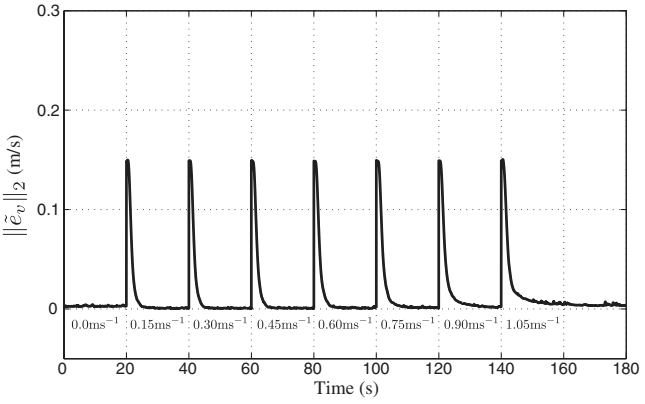

Fig. 21 Error-signal norm, $\|\tilde{e}_v\|_2$, using controller designed for multiple operating points.

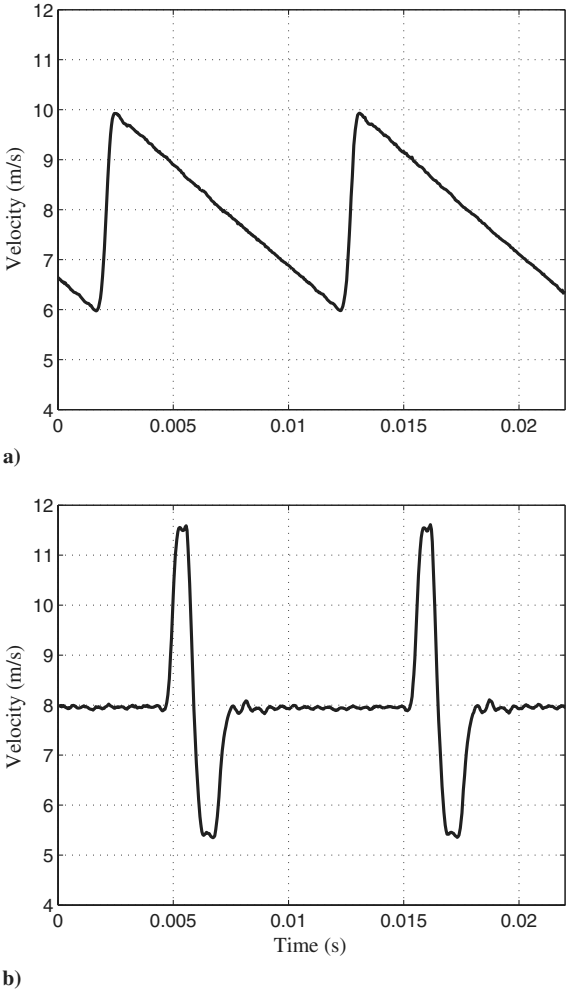

Fig. 22 Example a) sawtooth waveform and b) doublet waveform.

C. Alternative Waveforms

Alternatives to pulsed-jet injection may be explored with the harmonic-coupling control system. For example, Fig. 22 shows the ability to track sawtooth and doublet waveforms at an amplitude of $V_{\text{rms}} = 1.0\ \text{ms}^{-1}$ and $\omega_0 = 100$ Hz. The doublet waveform contains two successive pulses: one above the mean and one below the mean. The properties of these waveforms may be better suited for specific applications of pulsed-jet injection when compared to periodic square pulses. For example, the doublet waveform may perturb the flowfield to adhere, on average, closer to the injection wall, a benefit for film-cooling applications [27].

V. Conclusions

This paper presents the identification and control strategies for periodic waveform tracking in an experimental pulsed-jet-injection system. The main contribution is the introduction of demodulated signal components, in which scalar signals — the system input and output — are demodulated at the harmonic frequencies present in the Fourier series of the periodic reference waveform. The demodulated signals are low bandwidth and can be viewed as slowly varying amplitude variables for sinusoids at the harmonic frequencies. This change of coordinates, however, converts a single-input/single-output system into a MIMO system in which the off-diagonal elements reveal the coupling between different frequency bins. This point of view is uniquely suited to quantifying the nonlinear coupling between harmonics in the pulsed-jet experiment. It was demonstrated that the dc-gain matrices associated with linearizations performed in the demodulated coordinates at various operating points can be used for synthesizing stabilizing controllers that drive the jet velocity to asymptotically track the velocity-reference waveform within the bandwidth of the actuator and over a wide range of amplitudes up to incipient saturation of the actuator. Feedback of the jet velocity was facilitated by an inner loop, which acted on a pressure measurement taken from the plenum. Feedback of the pressure signal was useful for establishing operating points close to the desired periodic jet-velocity waveform. The inner loop also has an equalizing effect on the jet-velocity components, which produces lower condition numbers of the dc-gain matrices.

There is no doubt as to the utility of this approach for nonlinear plants, but future research can put the modulation–demodulation control approach on a more firm theoretical foundation where nonlinear plants are concerned. Proofs that go beyond local stability in a neighborhood of an operating point are still lacking and would require global models of the system, which is an additional challenge in itself. Furthermore, it is also not known under what conditions the structure (8) of the linearizations conforms to what was empirically noted. This structure was only exploited for identification of the dc-gain matrices, but not for controller synthesis. With regard to controller synthesis, the authors only touched on a few of many potentially viable approaches. For example, the conservatism of the authors' synthesis formulation can be reduced by introducing additional decision variables that correspond to similarity transforms of the closed-loop-dynamics matrix that also attempt to reduce its maximum singular value, although in this case the problem becomes nonconvex. It is also possible to embed the identified plants in a more general uncertainty description for which many analysis and synthesis tools exist [26]. Finally, the authors noted in their experiments the presence of significant out-of-band harmonics that cannot be directly regulated by the controller due to the fact that they lie beyond the actuator bandwidth. Nevertheless, these harmonics are a consequence of the in-band forcing, and so another direction to pursue is a means of adjusting the reference waveform so as to manipulate the out-of-band harmonics to enhance the features of the waveform that are critical for the flow-control study. Future publications will address these challenges.

Acknowledgments

The authors gratefully acknowledge the financial support from the National Science Foundation (NSF) and the advice of their colleague, Ann Karagozian. This work is sponsored by the NSF under grant number CBET-0755104.

References

[1] Margason, R. J., "Fifty Years of Jet in Crossflow Research," AGARD, CP-534, 1993, pp. 1–141.

[2] Karagozian, A. R., "Transverse Jets and Their Control," *Progress in Energy and Combustion Science*, Vol. 36, No. 5, 2010, pp. 531–553. doi:10.1016/j.pecs.2010.01.001

[3] Vermeulen, P. J., Grabinski, P., and Ramesh, V., "Mixing of an Acoustically Excited Air Jet with a Confined Hot Crossflow," *Journal of Engineering for Gas Turbines and Power*, Vol. 114, No. 1, 1992, pp. 46–54. doi:10.1115/1.2906306

[4] Bons, J. P., Sondergaard, R., and Rivir, R. B., "The Fluid Dynamics of LPT Blade Separation Control Using Pulsed Jets," *Journal of Turbomachinery*, Vol. 124, No. 1, 2002, pp. 77–85. doi:10.1115/1.1425392

[5] Johari, H., Pacheco-Tougas, M., and Hermanson, J. C., "Penetration and Mixing of Fully Modulated Turbulent Jets in Crossflow," *AIAA Journal*, Vol. 37, No. 7, 1999, pp. 842–850. doi:10.2514/2.7532

[6] M'Closkey, R. T., King, J., Cortelezzi, L., and Karagozian, A. R., "The Actively Controlled Jet in Crossflow," *Journal of Fluid Mechanics*, Vol. 452, Feb. 2002, pp. 325–335.

[7] Shapiro, S., King, J., M'Closkey, R. T., and Karagozian, A. R., "Optimization of Controlled Jets in Crossflow," *AIAA Journal*, Vol. 44, No. 6, 2006, pp. 1292–1298. doi:10.2514/1.19457

[8] Davitian, J., Hendrickson, C., Getsinger, D., M'Closkey, R., and Karagozian, A., "Strategic Control of Transverse Jet Shear Layer Instabilities," *AIAA Journal*, Vol. 48, No. 9, 2010, pp. 2145–2156. doi:10.2514/1.J050336

[9] Johari, H., "Penetration and Mixing of Fully Modulated Turbulent Jets in Crossflow," *AIAA Journal*, Vol. 44, No. 11, 2006, pp. 2719–2725. doi:10.2514/1.18929

[10] Francis, B. A., and Wonham, W. M., "The Internal Model Principle for Linear Multivariable Regulators," *Applied Mathematics & Optimization*, Vol. 2, No. 2, 1975, pp. 170–194 doi:10.1007/BF01447855

[11] Tsao, T. C., and Tomizuka, M., "Robust Adaptive and Repetitive Digital Tracking Control and Application to a Hydraulic Servo for Noncircular Machining," *Journal of Dynamic Systems, Measurement and Control*, Vol. 116, No. 1, 1994, pp. 24–32. doi:10.1115/1.2900676

[12] Tzou, Y. Y., Ou, R. S., Jung, S. L., and Chang, M. Y., "High-Performance Programmable AC Power Source with Low Harmonic Distortion Using DSP-Based Repetitive Control Technique," *IEEE Transactions on Power Electronics*, Vol. 12, No. 4, 1997, pp. 715–725. doi:10.1109/63.602567

[13] Chew, K. K., and Tomizuka, M., "Digital Control of Repetitive Errors in Disk Drive Systems," *IEEE Control Systems Magazine*, Vol. 10, No. 1, 1990, pp. 16–20. doi:10.1109/37.50664

[14] Lau, K., Goodwin, G. C., and M'Closkey, R. T., "Properties of Modulated and Demodulated Systems with Implications to Feedback Limitations," *Automatica*, Vol. 41, No. 12, 2005, pp. 2123–2129. doi:10.1016/j.automatica.2005.07.009

[15] Lau, K., Quevedo, D. E., Vautier, B. J. G., Goodwin, G. C., and Moheimani, S. O. R., "Design of Modulated and Demodulated Controllers for Flexible Structures," *Control Engineering Practice*, Vol. 15, No. 3, 2005, pp. 377–388. doi:10.1016/j.conengprac.2005.09.004

[16] Kandil, T. H., Khalil, H. K., Vincent, J., Grimm, T. L., Hartung, W., Popielarski, J., York, R. C., and Seshagiri, S., "Adaptive Feedforward Cancellation of Sinusoidal Disturbances in Superconducting RF Cavities," *Nuclear Instruments and Methods in Physics Research*, Vol. 550, No. 3, 2005, pp. 514–520. doi:10.1016/j.nima.2005.05.060

[17] Byl, M. F., Ludwick, S. J., and Trumper, D. L., "A Loop Shaping Perspective for Tuning Controllers with Adaptive Feedforward Cancellation," *Precision Engineering*, Vol. 29, No. 1, 2005, pp. 27–40. doi:10.1016/j.precisioneng.2004.04.005

[18] Hendrickson, C., and M'Closkey, R. T., "Phase Compensation Strategies for Modulated–Demodulated Control with Application to Pulsed Jet Injection," *Journal of Dynamic Systems, Measurement and Control*, Vol. 134, No. 1, 2011, Paper 011024. doi:10.1115/1.4004768

[19] xPC Target, *xPC Target User's Guide*, The MathWorks, Natick, MA, 2004.
[20] Megerian, S., Davitian, J., de B. Alves, L. S, and Karagozian, A. R., "Transverse Jet Shear Layer Instabilities. Part 1. Experimental Studies," *Journal of Fluid Mechanics*, Vol. 593, Dec. 2007, pp. 93–129. doi:10.1017/S0022112007008385
[21] Davitian, J., Getsinger, D., Hendrickson, C., and Karagozian, A. R., "Transition to Global Instability in Transverse-Jet Shear Layers," *Journal of Fluid Mechanics*, Vol. 661, Oct. 2010, pp. 294–315. doi:10.1017/S0022112010003046
[22] Hendrickson, C., and M'Closkey, R. T., "Dynamic Phase Compensation in Modulated–Demodulated Control for Pulsed Jet Injection," *Proceedings of the American Control Conference*, IEEE Publ., Piscataway, NJ, 2011, pp. 3053–3058.
[23] Pintelon, R., and Schoukens, J., *System Identification: A Frequency Domain Approach*, IEEE Press, New York, 2001.
[24] Skogestad, S., and Postlethwaite, I., *Multivariable Feedback Control: Analysis and Design*, Wiley, Chichester, England, U.K., 1996.
[25] Chen, C.-T., *Linear System Theory and Design*, 3rd ed., Oxford Univ. Press, New York, 1998.
[26] Packard, A., Balas, G., Safonov, M., Chiang, R., Gahinet, P., Nemirovski, A., and Apkarian, P., *Robust Control Toolbox*, The MathWorks, Natick, MA, 2012.
[27] Ekkad, S. V., Ou, S., and Rivir, R. B., "Effect of Jet Pulsation and Duty Cycle on Film Cooling from a Single Jet on a Leading Edge Model," *Journal of Turbomachinery*, Vol. 128, No. 3, 2006, pp. 564–571. doi:10.1115/1.2185122

E. Gutmark
Associate Editor